Effect of twins in Ni substrates on the microstructure of La2Zr2O7 films for coated conductors

Sarah Petit, Sébastien Pairis, Mélissa Mikolajczyk, Luc Ortega, Jean-Louis Soubeyroux, Philippe Odier

Effect of twins in Ni substrates on the microstructure of $La_2Zr_2O_7$ films for coated conductors

Sarah Petit[1,2**], Sébastien Pairis[2], Melissa Mikolajczyk[1,2], Luc Ortega[2***], Jean-Louis Soubeyroux[1,2*], Philippe Odier[1,2]

1 CRETA-CNRS, 25 av. des Martyrs, BP166, 38042 Grenoble Cedex, France

2 Institut Néel-CNRS, 25 av. des Martyrs, BP166, 38042 Grenoble Cedex, France

* Corresponding author: jean-louis.soubeyroux@grenoble.cnrs.fr

** Now at LETI, CEA Grenoble.

***Now at Laboratoire de Physique des Solides, Université Paris, Orsay, France

Abstract

$La_2Zr_2O_7$ (LZO) films were deposited by chemical solution deposition on $Ni_{95}W_5$ Rolling Assisted Bi-axially Textured substrates to be used in $YBa_2Cu_3O_7$ (YBCO) coated conductors. These LZO films were proved of good qualities for YBCO deposition by Metal Organic Chemical Vapour Deposition that is an economic process. The mosaic of LZO films is only slightly degraded by the process of grain-to-grain epitaxial transfer (16% with respect to that of the substrate). The film is composed of small crystallites (20 - 40 nm) and larger anomalous crystallites (100 - 400 nm) found in great number in transferred twins from the substrate. The

anomalous crystallites are poorly crystallised or amorphous and contain more C than areas with normal crystallites. High temperature in-situ X ray shows a sudden crystallisation at 860°C that does not seems to involve a solid state reaction. The anomalous crystallites are analysed to result from a locally enhanced barrier to nucleation and might reveal sor characteristics of the crystallization.

Keywords : epitaxy, film, microstructure, **$La_2Zr_2O_7$**

I. Introduction

Many examples of buffer layer made of $La_2Zr_2O_7$ oxide (LZO) have been studied by chemical solution deposition (CSD) on highly bi-axially textured Ni-5at %W ($Ni_{95}W_5$) substrates [1-6] obtained by the so called Rolling Assisted Bi-axially Textured technique (RABIT). LZO acts as a barrier against diffusion of the Ni toward YBCO [7, 8] and must limit the oxidation during the different steps of the synthesis process of the coated conductor [9, 10]. This buffer layer is used as a template to grow epitaxially the superconducting layer made of $YBa_2Cu_3O_7$ (YBCO) and for example deposited by Metal Organic Chemical Vapour Deposition (MOCVD) [11-16]. We focus on a simplified architecture composed of only one substrate, one buffer layer in LZO and one YBCO superconducting layer. This choice is made with the perspective of making an economic process. Using the combination of CSD for the buffer and MOCVD for the YBCO, critical currents reaching or exceeding 1 MA/cm^2 (self field at 77 K) have been obtained on Ni RABIT substrates. In MOCVD deposited YBCO on Ion Beam assisted Deposition (IBAD) structures, although the process is being much more advanced, a limitation to the current flow has been recently analysed to be caused by **a**-axis growth [17]. We also have observed similar phenomenon on our MOCVD deposited YBCO samples made on a single LZO buffer layer, see fig.1. It is interesting to notice that these **a**-axis growths are not restricted to YBCO MOCVD on IBAD substrates but are also observed when YBCO is deposited on RABIT substrates by reel-to-reel pulsed laser deposition [18].

The development of coated conductors requires attention to these defects. Their origin is not clear but is frequently assigned to a too low YBCO processing temperature; however it should be questioned whether it could be issued from the buffer itself. It is then necessary to identify all possible sources of defects in the buffer that could induce such disoriented grains.

Compared to more complexes architectures generally used (involving up to 5 or 6 intermediate layers), line ending with defects in the buffer layer is expected to be more prominent. Rikel et al. [13] have shown the importance of the quality of the buffer layer in this case where one LZO buffer on Ni RABIT substrate is covered with YBCO deposited by MOCVD.

LZO (a cubic structure with a 7.7 % structural mismatch with $Ni_{95}W_5$) grow by epitaxy on $Ni_{95}W_5$ after a rotation of 45° of its unit cell for better matching the substrate lattice [19]. Due to this property, many papers show that LZO reproduces exactly the grain morphology of the substrate obtained by the RABIT process [20]. The microstructure of LZO is made of small rounded crystallites (20-50 nm) with nanovoids [7] originated from the released gases in the CSD process under Ar-5% H_2 [21], but the crystallization process made these voids cubic [8]. The grain boundaries of the Ni substrate are transferred to the LZO microstructure by the epitaxial process giving rise to the typical grain morphology mentioned above. Twins that are present in the substrates are also reproduced in the LZO microstructure and an example is shown in the following (see fig.2 with a transferred twinned grain visible in the center of the image). Many authors have attempted to optimize composition and annealing procedure of their rolled substrate in order to maximize the cube texture content and to minimize the residual twins because twins are considered as defects expected to inhibit epitaxial growth. However, very few publications have verified this fact (see for example ref [22]).

The aim of this work is to investigate peculiarities of the microstructure of LZO buffer layers grown on $Ni_{95}W_5$ by CSD. This paper focuses on grains transferred from twins in the substrate and observed by Secondary Electron Microscopy (SEM), Electron Backscattering Scanning Diffraction (EBSD) and Emission Dispersion X ray spectroscopy (EDX) techniques. It is discovered that these grains are composed of anomalous crystallites that are also detected,

sometimes, inside grains where most of the LZO crystallites are normal. The occurrence of these anomalous crystallites is discussed considering the nucleation of LZO with the help of in-situ X ray diffraction at high temperature.

Experimental details

$Ni_{95}W_5$ RABIT substrates were received from Evico's company (Dresden-Germany) and coated after cleaning in acetone and methanol for 15 min each in an ultrasonic bath. The substrates (typically 5 cm long) were covered with LZO according to a procedure where the propionic precursors of La and Zr are synthesized first separately [23], then mixed (1:1) at 60°C for 1 h with propionic acid to a concentration of 0.6 M. This solution was used to dip-coat the samples at a withdrawal speed of 66 mm/min. After drying and crystallization at 960°C in Ar-5%H_2 forming gas, the thickness of the film was ~ 70 nm [10]. The film thickness was measured by optical means and controlled by microscopy on cross section obtained by ion milling.

Texture of both substrates and LZO films were obtained by X-ray diffraction (Cu K_α) with a Seifert MZ-VI in the Schultz geometry. The beam size (horizontal 0.8 mm x vertical 2 mm) is defined by an appropriate collimating multilayer optics from Xenocs (Grenoble-France) which provides a parallel beam (divergence of 0.06°). A graphite analyzer coupled to a point detector (NaI) collects the diffracted intensities with a very high signal/noise ratio ($>10^5$). Measurement of the direct beam and careful sample alignments were performed before each measurement allowing valuable comparisons between samples.

In situ X-ray diffraction versus temperature (called further "in situ HT X-ray") was performed with a Brucker Advance D8 diffractometer working at the wavelength of CuKα and equipped with a heating stage protected with a graphite dome allowing measurements of

asymmetric reflections. The furnace was flushed with He-5%H_2 and both (222) and (400) reflections of LZO were recorded quasi simultaneously versus temperature thanks to a fast Vantek positive sensitive detector. The heating temperature schedule (heating 300°C/h, dwell 60 min at 960°C) was selected to be as close as possible as the one used in the films' crystallization.

SEM images have been performed using a Field Emission Scanning Electron Microscope (FESEM) from Zeiss Ultra+ (Zeiss, Germany) equipped with an EBSD unit using "HKL" indexing software (Oxford Instruments) and an EDX spectrometer from Bruker. SEM images were taken at low operating voltage, 3kV, to have more sensitivity to the surface details. EDX spectra were obtained on a silicon drift detector Bruker 4010 (SDD) used with a thin window Moxtek AP3.3 (x-ray transmittance for carbon line of about 46%). The SDD detector has an energy resolution of 51eV for C-Ka, 57eV for O-Ka and 124eV for Mn-Ka. The analyses were done with a 8mm working distance, a take-off angle of 35°, a measure time analysis of 100s (with a dead time less than 2%), at 5kV. Atomic Force Microscopy (AFM) images were acquired with a Veeco D3100 and a Nanoscope V controller, operating in a tapping mode with Si tip (radius 10 nm) at ambient conditions.

Thermal analysis was performed with a SETARAM (Lyon, France) TAG1600 flown with Ar and allowing measurements up to 1600°C with a high sensitivity (µg). The occurrence of two symmetrical furnaces allows avoiding gas density corrections. The TAG1600 is equipped with a differential thermal analysis modulus enabling to measure simultaneously weight variations and thermal analysis. It uses two crucibles made in alumina (150 µl), one is used as a reference and the other for the sample (a few mg).

II. Results

The deposited LZO films were crystallized according to a process close to the one described in ref [6]. This process involves a pyrolysis step under vacuum that allows an efficient elimination of organic solvents in the temperature range 350°C. It is composed of a ramp under vacuum up to 350°C (550°C/h) followed by a dwell of 60 min and then a crystallization step involving a ramp up to 960°C followed by a dwell of 30 min under Ar – 5 %H_2 flow (5 l/min). This treatment provides reproducible results concerning the texture. On a series of 35 samples, the average in-plane misorientation was $\Delta\phi = 7.0° \pm 0.7°$ and out of plane misorientation was $\Delta\omega = 6.3° \pm 0.6°$ RD and $\Delta\omega = 10.4° \pm 1.5°$ TD respectively. Compared to Ni misorientation, the ratio $(\text{misorientation})_{LZO}/(\text{misorientation})_{Ni}$ was constant and equal to 1.16, revealing only a small degradation of the texture transferred to the buffer by grain-to-grain epitaxy. Moreover, this process gives crystallized films up to their ultimate surface as probed by EBSD. Similar results were observed at Nexans Hürth [24]. Figure 3~~2~~ shows the overall microstructure observed by SEM with well visible grains transferred from Ni substrate. Some grain boundaries are more marked than others. The different grey levels are related to variations of orientation of the different grains which are easily quantified by EBSD (not shown) and correspond to the out of plane and/or in-plane deviations also revealed by X-ray diffraction. Figure 2~~3~~ shows a zoom of another sample of the same series with a twin transferred from the Ni substrate in the center of the image. Twins in substrates are originated from the recrystallisation process of the substrate [25].

To get information about the individual crystallites of LZO, zoomed pictures of the surface have been obtained by SEM and AFM, with the advantage in this case to get 3D information. The images of fig.4 show typical features of LZO microstructure; in our case it is

mainly composed of rounded crystallites (20-40 nm) with some additional larger crystallites, see fig.4b and fig.5. In the following we shall distinguish between grains transferred from substrate and crystallites of LZO developed during the crystallization of the film. The larger crystallites are in rather small number in this portion of the sample. Analysis of their surface, insert of fig.5, shows clearly that these large crystallites possess low surface roughness and are underdeveloped crystallites in comparison to normal crystallites (their surface is 3 nm below the mean surface of the normal grains). The overall roughness is in the range of 2 nm, i.e. smaller than the depth of the anomalous crystallites below the surface. These anomalous crystallites are 4-10 times larger than the normal crystallites, with sizes reaching 400 nm, they have not been discussed so far in literature, although some reports do show their finger print [7,26]. We have also observed these anomalous crystallites in LZO films produced at Nexans-Hürth (Germany) and more recently on LZO coated substrates from AMSNA. Curiously, it was observed that some grains do not contain any anomalous crystallites while, for unknown reasons, an adjacent grain could contain several or even many. Their aspect is also variable as is shown fig.6 by SEM. In this figure, different portions have been underlined to guide eyes. Portion denoted **(a)** appears "amorphous like" with no contrast inside the anomalous crystallite. Portion denoted **(b)** shows normal crystallites (typical size of 20-40 nm), grouped in colonies having an identical size and shape than the anomalous crystallites **(a)**. Notice that the frontier between colonies disappears in grains where no anomalous crystallites are visible. Portion **(c)** denotes areas which are intermediate between **(a)** and **(b)**. This suggests that a transformation between "amorphous like" to "crystallized like" exists within the time scale of the annealing, that is a rather slow kinetic. Because these anomalous crystallites have rather small sizes, it was not easy to determine for sure their crystallization state by EBSD nor their chemical composition by EDX. Zones containing high concentration of such anomalous crystallites were then searched.

Anomalous crystallites are observed with a high concentration in ~~of~~ twins transferred grains, as shown in fig.7, part a. Part b of this figure shows a zoomed picture of such transferred twin. These anaomalous crystallites have the same typical morphological features than those detailed previously. Note that the adjacent grains, which are not twinned, do not contain anomalous crystallites. X-Ray diffraction has been acquired on these films, with the aim to identify, if possible, the crystallization state of transferred twin grains. Figure 8 compares the contribution of the substrate (pole figure of Ni(111) reflection, part a) to that of the LZO film (pole figure of LZO(222) reflection, part b) deposited on top of it. These pictures show raw data plotted in log scale with the same criterion: the intensity levels are separated with the same interval of intensity to give a similar representation. The substrate shows the typical behavior of a cube texture plus diffracted intensities for tilted angles in the range χ = 0-20° which is typical of contributions from twinned grains of the Ni matrix [27]. In comparison, LZO film's pole figure shows intense contribution at χ = 54.7° of the cube texture and small distributed contributions elsewhere. For LZO crystallized on the twinned area one expect spots in a crown around χ = 16°. No such spot are visible suggesting perhaps amorphous grains.

A typical twinned area was then investigated by EBSD to provide information concerning the crystallization of the surface (10-20 nm in depth) and on its orientation. A SEM image of the area, tilted at 70° from the normal to the sample, is shown in part 1 of fig.9. It evidences the presence of a twinned area that is underlined by the dotted line. An EBSD image of this area is shown in part 2 of fig.9 where the different color encodes rotations around the normal of the grains with the Euler angles coordinates. Black encoding is for non-indexed parts, i.e. areas where either no Kikuchi lines are discernible or cannot be indexed. In our case, the underlined area does not show visible Kikuchi lines (no diffraction) despite the fact that it is covered with the same thickness of LZO than elsewhere (this was deduced from the evolution of the EDX

intensity of Zr and La peaks in a profile made across a twinned area). Note that adjacent grains show the typical Kikuchi lines of LZO crystallites. The loss of observable Kikuchi pattern in anomalous crystallites was then checked in grains containing isolated anomalous crystallites. It was confirmed that the Kikuchi lines disappears in many anomalous crystallites but not for all of them; some are crystallized but with different orientations with respect to the majority of crystallites.

To get some insight in the chemistry involved in the inhibition of the crystallization of anomalous crystallites, local chemical analyses were performed. It was not possible to get any difference between an anomalous crystallite and normal crystallites because of the spatial resolution of the EDX measurement. We then measured a twinned area containing many anomalous grains assuming it to be representative of the anomalous crystallites. A composition profile across a grain and an adjacent twin does not show any anomaly for Zr, La, O, Ni. Investigation of the carbon content reveals some interesting differences. The C level is systematically higher, up to four times more, in the twinned area compared to the normal area, as shown in fig.10. A comment concerning the carbon detection must be made here. Although, the voltage was limited to 5 kV (compared to 20 kV often used) to favor ionization of low energy lines and limit the contribution of the substrate, cracking of the residual atmosphere by the electron beam is a major phenomenon resulting in the deposition of carbon under the spot of the electron beam. It can be seen (points 19, 20 and others) on fig.10. The kinetic of deposition is interesting to follow: it is composed of a first rapid step followed by a slow one. The first step is due to the carbon contained in the film while the slow step is due to the progressive carbon contamination from the residual atmosphere. In the twinned area, the contribution of film's contained carbon is much larger than elsewhere in normal crystallites areas. This observation was repeated several times on several twinned areas.

Finally, the crystallization of the film was investigated with the aim to get insight into the nucleation mechanism. The in-situ HT X-ray system allows to record (400) and (222) reflections from LZO versus temperature quasi simultaneously. On fig.11, the diffracted intensity versus Bragg angle is represented in a 2D plot when the sample surface was set vertical (i.e. parallel to the X-ray diffusion vector). The temperature cycle is superimposed in red and refers to right and upward scales. The main contribution arises from Ni (200) reflection at $2\theta = 51.5°$ which is insensitive to heating except small shifts due to thermal expansion. This is the position expected for $Ni_{95}W_5$ (a = 3.541 Å). This reflection is accompanied by a reflection at $2\theta \sim 33°$ observed when the temperature is above T = 860°C, it is due to (400) Bragg planes of LZO growing parallel to the substrate. Weak reflections are due to AlN support and parasitic diffraction induced by the graphite dome. Fig.11 shows a similar image but for the sample tilted at $\chi = 54.7°$ from vertical and then in position to make (222) LZO planes to diffract. As a consequence, fig.11 is marked by a unique feature at $2\theta \sim 29°$ corresponding to (222) planes appearance. The exact angles are consistent with the unit cell parameter of LZO (a = 10.786 Å). The threshold for the onset of this diffraction is observed at the same temperature as for (400) planes. This confirms the epitaxial growth of LZO on $Ni_{95}W_5$ substrate from in situ X ray at high temperature. Although, this is not new, the high temperature (860°C) of crystallization and its sudden onset is surprising considering the early mineralisation of ZrO_2 observed at 450°C according to thermal studies on the decomposition of Zr propionates [23]. In our case, although Zr propionate was mixed with La propionate to form the precursor for LZO deposition, the thermal weight evolution measured previously [28] is consistent with the early formation of ZrO_2 ~~[25]~~. As a consequence, LZO synthesis was expected to involve a solid state reaction between ZrO_2 and La_2O_3 or more probably an oxycarbonate of this oxide. Effectively, the thermal decomposition of La acetylacetonate involves the intermediate formation of an oxycarbonate, and we have observed

that the decomposition of La propionate also involves a step with oxycarbonate [29], see figure 12. According to this, the mixture ZrO_2 + oxycarbonate remain amorphous up to a rather unexpected high temperature (860°C). The very high under-cooling of such amorphous films may justify a high temperature of nucleation as observed here [30].

Discussion

The observation of locally amorphous crystallites or even amorphous areas in crystallized buffer layers is of importance since they are sources of defects in the YBCO layer to be deposited on top. This is even more important in the present case of a simple architecture composed of only one buffer layer. Because YBCO nucleates on the top surface of the buffer, amorphous areas will become zones where homogeneous nucleation or **a** axis nucleation will take place because they have lower energy barrier to nucleation. These non orientated **c** axis areas are non favorable orientations for super-current flow and source of current limitation. Unfortunately, we have presently no correlation with the **a** axis content and Jc, we just know that it limits the current flow [17]. This is also a big challenge to correlate **a** axis growth to defects of the buffer layer. We just know for the moment, from cross sections studies, that **a** axis growth can appear from the buffer and go across the entire YBCO layer (not shown).

The observation of areas where crystallization is absent is surprising considering the high temperature used for crystallization, i.e. 960°C, that is 100°C above the crystallization onset measured here and confirms previous measurements made with equipments measuring only symmetrical lines and not able to ascertain the epitaxial growth directly [31,32]. This proves that the energy barrier to nucleation was higher in these areas than elsewhere and has not been overcome with the temperature used. In confirmation, recent experiments show that heating at a higher temperature; i.e. 1000-1050°C, make these anomalous crystallites to disappear.

The anomalous grains, also amorphous, are underdeveloped grains which surface remains below the surface of normal crystallites. This gives an insight in the crystallization process. When the crystallization occurs, one can anticipate that a 3D grows starts with the creation of voids and a redistribution of the solid matter. In this viewpoint, voids observed by many persons in LZO film produced by CSD would have their origin in the crystallization mechanism more likely than in gas release. This is still an open question.

In twinned area (with frequent orientation (122)), due to crystallographic strains, the nucleation of (200) planes is highly improbable and the LZO remains amorphous on top or crystallized locally with a random orientation due to homogeneous nucleation. Patches of un-crystallized LZO on normal grains of Ni is more difficult to understand and suggests that some properties of the interface are in cause. More efforts have to be done in this direction in the future to make the buffer layer more reliable and exempt of deficient zone.

III. Conclusion

Amorphous crystallites have been found in LZO films processed by CSD technique. These crystallites are due to a higher barrier for nucleation than for normal crystallites that is not overcome by the processing temperature used here. Amorphous crystallites are in high concentration on twin zone transferred from the substrate and found sporadically on normal grains transferred by grain-to-grain epitaxy from the substrate. Reducing the number of twins is an obvious conclusion already taken in charge by the substrates manufacturers. Moreover, identification of the reason for locally inhibited nucleation is important if one wants to decrease the processing temperature and take benefit of the large temperature range (100°C) that exists between the actual processing temperature and the crystallization temperature.

IV. Acknowledgments

The authors wish to thank the Cluster MACODEV of Rhône-Alpes Region (France) for supporting equipment acquisition, FEDER European funds and AMSNA for supporting salaries for Dr S. Petit and M. Mikolajczyk and Nexans for supplying LZO films deposited on $Ni_{95}W_5$ RABIT substrates. Dr O. Stadel from Percotech is acknowledged for MOCVD deposition on LZO buffered Ni RABIT substrates.

VI. References

[1] S. Sathyamurthy, M. Paranthaman, T. Aytug, B.W. Kang, P.M. Martin, A. Goyal, D.M. Kroeger, D.K. Christen, J. Mater. Res. 17(2002)1543.

[2] K. Knoth, R. Hühne, S. Oswald, L. Schultz, B. Holzapfel, Acta Materialia 55(2007)517.

[3] H. Chen, R. Kumar, B. A. Glowacki, Materials Chemistry and Physics 122(2010)305.

[4] Y. Cheng, H. Suo, M. Gao, M. Liu, L. Ma, M. Zhou, Y. Ji, Acta Materialia 59(2011)2823.

[5] M. Paranthaman, S. Sathyamurthy, Xiaoping Li, E. D. Specht, S. H. Wee, C. Cantoni, A. Goyal, M.W. Rupich, Physica C 470(2010)352.

[6] V. Roche, C. Jimenez, P. Chaudouët, R. Benaboud, F. Weiss, E. Sarigiannidou, Thin Solid Films 520 (2012)2566.

[7] L. Molina, K. Knoth, S. Engel, B. Holzapfel, O. Eibl, Supercond.Sci.Technol. 19(2006)1200.

[8] L. Molina, H. Y. Tan, E. Biermans, K. J. Batenburg, J. Verbeeck, S. Bals , G. Van Tendeloo, Supercond. Sci. Technol. 24(2011)065019.

[9] Y. Wang, L. Zhou, Y. F. Lu, C. S. Li, Z. M. Yu, L. H. Jin, J. S. Li. J, Alloys and Compounds 509(2011)8812.

[10] S. Petit, M. Mikolajczyk, J. L. Soubeyroux, T. Waeckerlé, R. Batonnet, S. Pairis, P. Odier, IEEE Trans. on Applied Supercond. 21(2011)2977.

[11] T. Caroff, S. Morlens, A. Abrutis, M. Decroux, P. Chaudouet, L. Porcar, Z. Saltyte, C. Jimenez, P. Odier and F. Weiss, Supercond. Sci. Technol. 21(2008)075007.

[12] O. Stadel, R. Y. Muydinov, G. Braüer, M. Rikel, J. Ehrenberg, J. Bock, G. Kotzyba, R. Nast, W. Goldacker, S. V. Samoylenkov, A. R. Kaul, IEEE Trans.on Appl.Supercond. 19(2009)3160.

[13] M. Rikel, D. Isfort, M. Klein, J. Ehrenberg, J. Bock, E. D. Specht, M. Sun-Wagener, O. Weber, D. Sporn, S. Engel, O. de Haas, R. Semerad, M. Schubert, B. Holzapfel, IEEE Trans. on Applied Supercond.19(2009)3307.

[14] O. Stadel, R. Muydinov, H. Keune, J.Shmidt, A. Blednov, G. Dosovitsky, S. Samoylenkov, O. Gorbenko, A. Kaul, G. Kotzyba, R. nast, W. Goldaker, Journal of Physics: conf Series 97(2008)012158.

[15] O. Stadel, R. Muydinov, G. Braüer, M. Rikel, J. ehrenberg, J. Bock, G. Kotzyba, R. Nast, W. Goldacker, S. Samoylenkov, A. R. Kaul, IEEE Trans. Appl. Supercond. 19(2009)3160.

[16] A. Molodyk, M. Novozhilov, S. Steet, L. Castellani, A. Ignatiev, IEEE Trans. Appl. Supercon. 21(2011)3175.

[17] Pei Li, D. Abraimo, A. Xu, D. Larbalestier, Supercond. Sci. Technol.25(2012)025002.

[18] Y. Li, L. liu, H. Liu, X. Sun, D. Hong, D. Xu, Y. Wang, IEEE Trans. Appl. Supercond. 21(2011)2924.

[19] L. Rapenne, C. Jimenez, T. Caroff, C. Million, S. Morlens, P. Bayle-Guillemeaud, F. Weiss, J. Mater.Res.24(2009)1480.

[20] K. Knoth, R. Hühne, S. Oswald, L. Schultz, B. Holzapfel, Supercond. Sci. technol.18(2005)334.

[21] V. Cloet, T. Thersleff, O. Stadel, S. Hoste, B. Holzapfel, I. Van Driessche, Acta Materialia 58(2010)1489.

[22] B. Wörz, A. Heinrich, B. Stritzker, Physica C 418(2005)107.

[23] S. Petit, S. Morlens, Z. M. Yu, D. Luneau, G. Pilet, J. L. Soubeyroux, P. Odier, Solid State Sci. 13(2011)665.

[24] M. O. Rikel, J. Ehrenberg, S. Mahachi, M. Klein, B. Hoppe, J. Schütz, J. Bock, IEEE Trans. on Applied Supercond.21(2011)2928.

[25] R. Nast, B. Obst, W. Goldacker, Physica C372-376(2002)733.

[26] K. Knoth, R. Hühne, S. Oswald, L. Molina, O. Eibl, L. Schultz, B. Holzapfel, Thin Solid Films 516(2008)2099.

[27] E. D. Specht, A. Goyal, D. F. Lee, F. A. List, D. M. Kroeger, M. Paranthaman, R. K. Williams, D. K. Christen, Supercond.Sci.Technol.11(1998)945.

[28] Z. M. Yu, P. Odier, L. Ortega, L. Zhou, P. X. Zhang, A. Girard, Mat.Sci.Eng.B 130(2006)126.

[29] R. W. Schwartz, T. Schneller, R. Waser, C R Chimie 7(2004)433.

[30] G. A. M. Hussein, H. M. Ismail, Powder Technology 84(1995)185.

[31] S. Sathyamurthy, M. Paranthaman, M.S. Bhuiyan, E.A. Payzant, D.F. Lee, A. Goyal, X. Li, U. Scoop, M. Rupich, IEEE Trans. Appl. Supercond.15(2) (2005)2974.

[32] S. Sathyamurthy, M. Paranthaman, H.Y. Zhai, S. Kang, T. Aytug, C. Cantoni, K.J. Leonatd, E.A. Payzant, H.M. Christen, A. Goyal, X. Li, U. Schoop, T. Kodenkandath, M. Rupich, J.Mater.Res.19(2004)2117.

Figure Captions

Fig.1 YBCO a-axis oriented grains have grown on a grain of Ni bi-axially textured covered by an epitaxial buffer layer of LZO. This is clear on the center of the figure. YBCO was deposited by MOCVD.

Fig.2 LZO on $Ni_{95}W_5$ with a twin (at center) transferred from the substrate.

Fig.3 Grain microstructure of LZO deposited on $Ni_{95}W_5$ RABIT substrate.

Fig.4 Microstructure of typical LZO grains by AFM.

Fig.5 An anomalous grain of fig.4a. Insert: height profile.

Fig.6 Aspect of different crystallites. Contour of colonies of grains has been highlighted by doted lines. a)Anomalous crystallite; b) colony of normal crystallites; c) intermediate crystallites.

Fig.7 Areas with twined grains showing high proportion of anomalous grains.

Fig.8 Pole figures for a LZO/ $Ni_{95}W_5$ buffer.

Fig. 9 SEM (tilt = 70°) and EBSD of a twinned area with normal adjacent grains.

Fig.10 Chemical analysis of a twinned area. a)SEM at 5 kV; b)local chemical analysis by EDX for a grain (spot 20) and a twin (spot 19).

Fig.11 Crystallization of a LZO film on $Ni_{95}W_5$ RABIT substrate followed by in-situ HT X-ray diffraction . The temperature schedule is indicated by the red line referring to the right scale. 1a) sample vertical (parallel to the diffusion vector of X ray beam); 1b) sample tilted at $\chi = 54.7°$ from the diffusion vector of X ray beam.

Fig.12 Thermal weight analysis/Differential thermal analysis of $La(prop)_3$ showing the intermediate formation of an oxycarbonate in the decomposition steps.

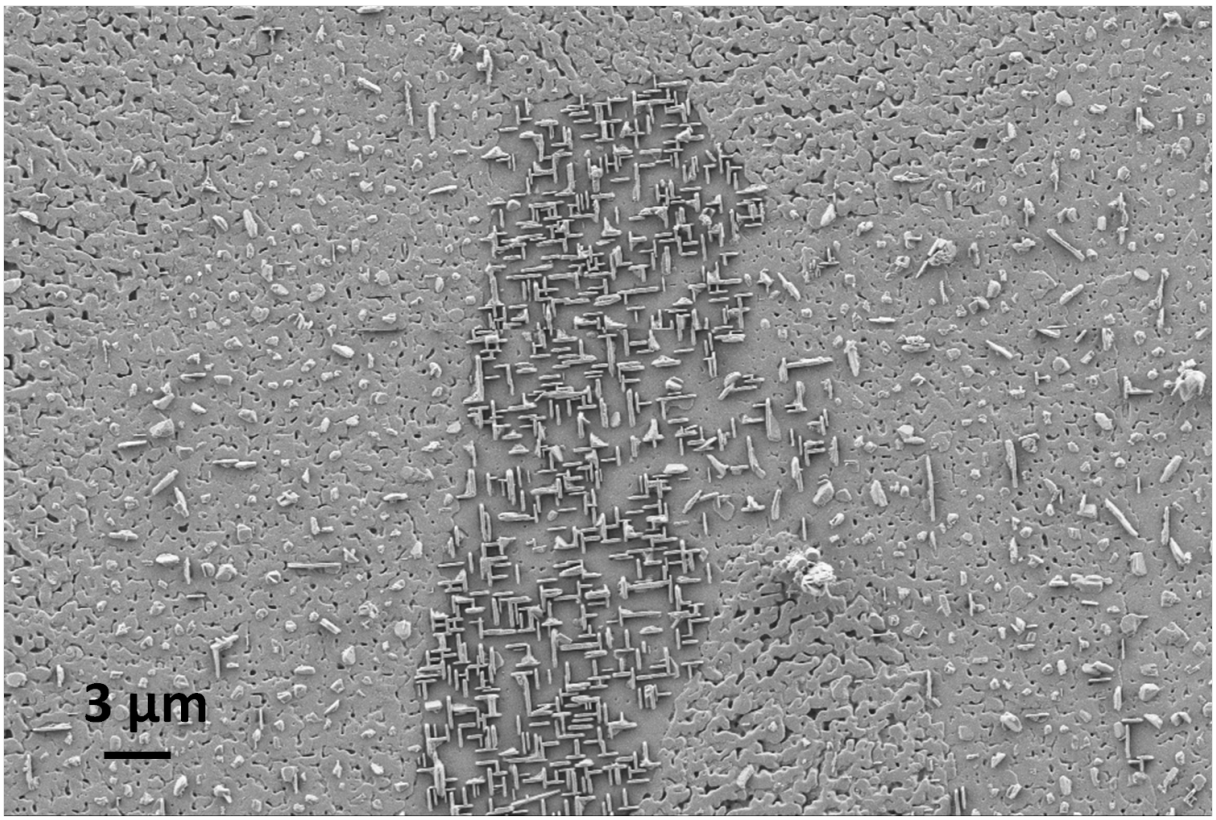

Fig.1

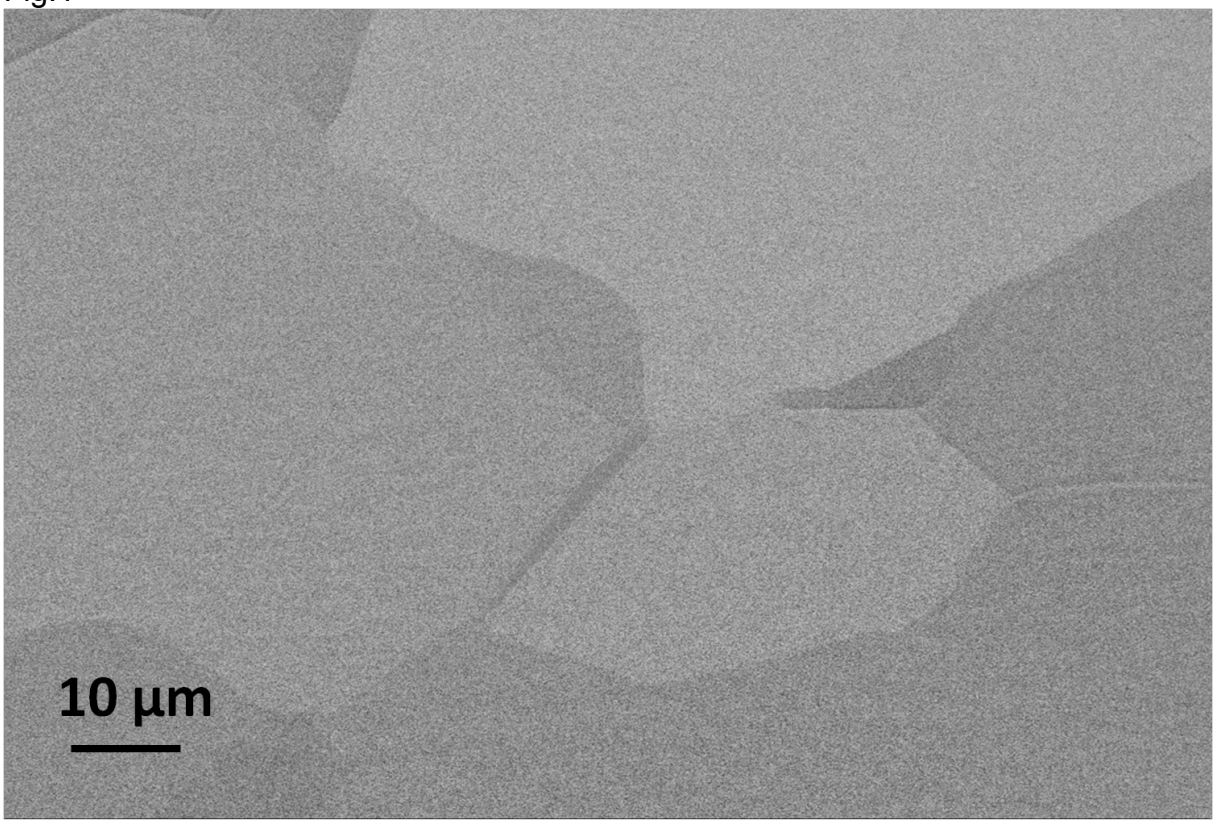

Fig.2

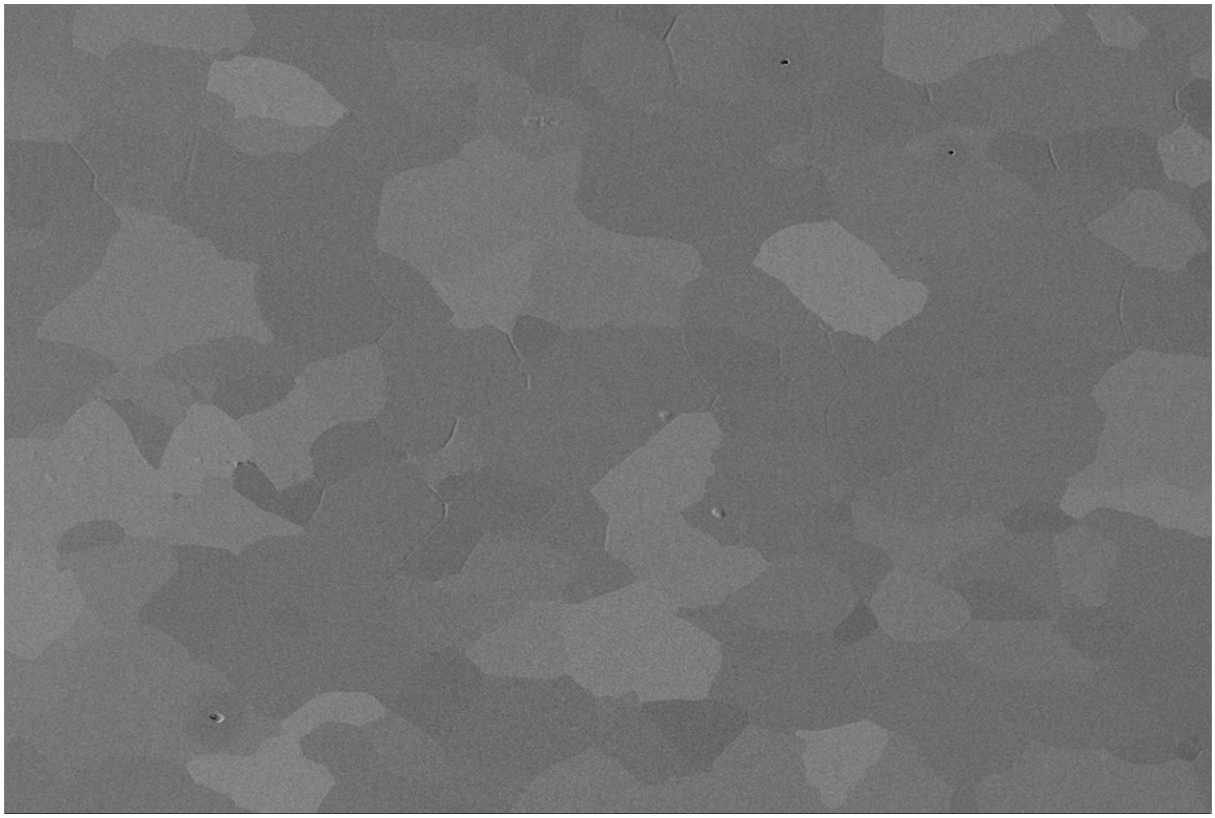

Fig.3

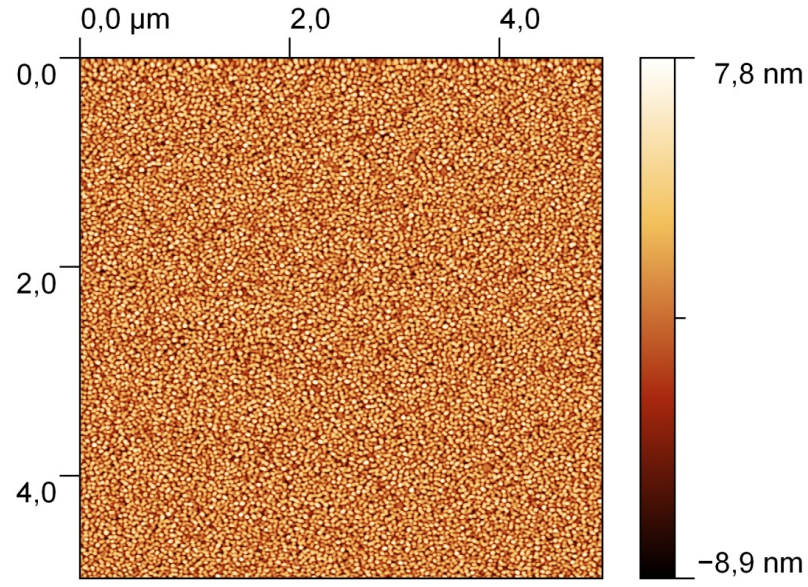

Fig4a

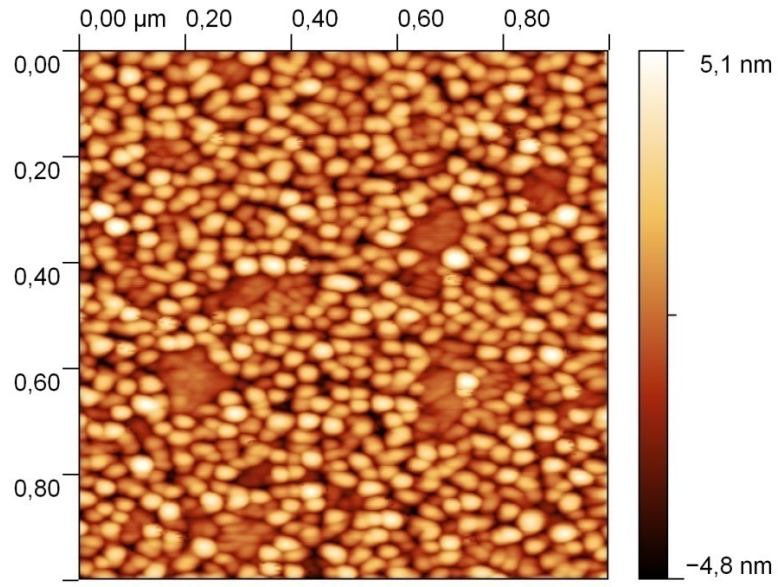
0,00 µm
0,20
0,40
0,60
0,80
0,00
0,20
0,40
0,60
0,80
5,1 nm
−4,8 nm

Fig.4b

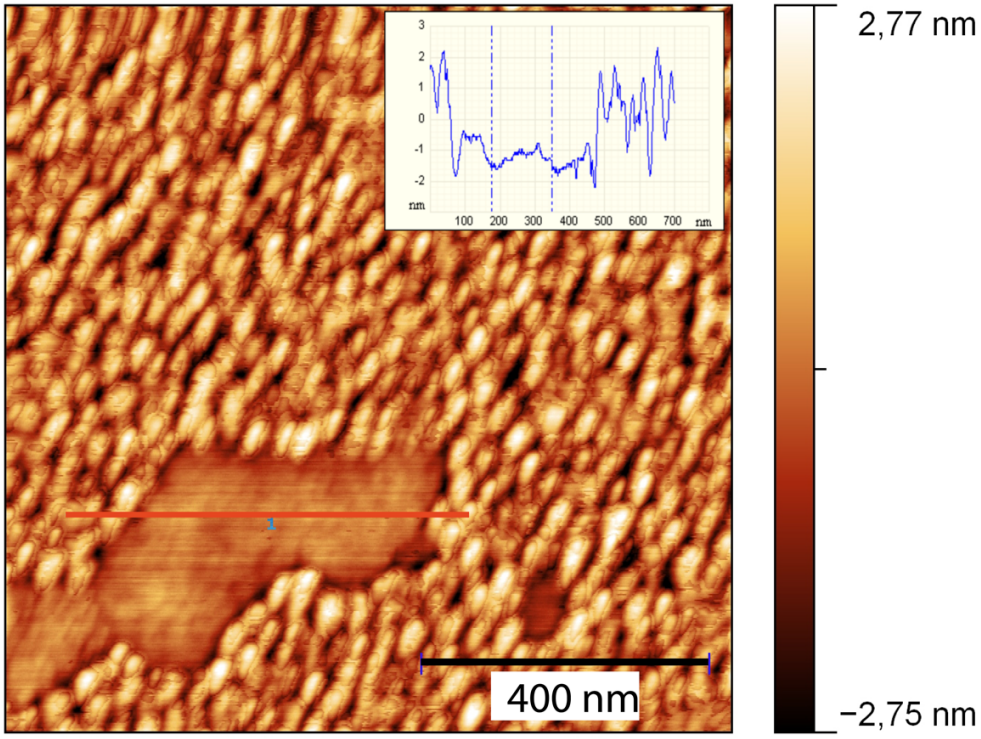
3
2
1
0
-1
-2
nm
100
200
300
400
500
600
700
nm
400 nm
2,77 nm
−2,75 nm

Fig.5

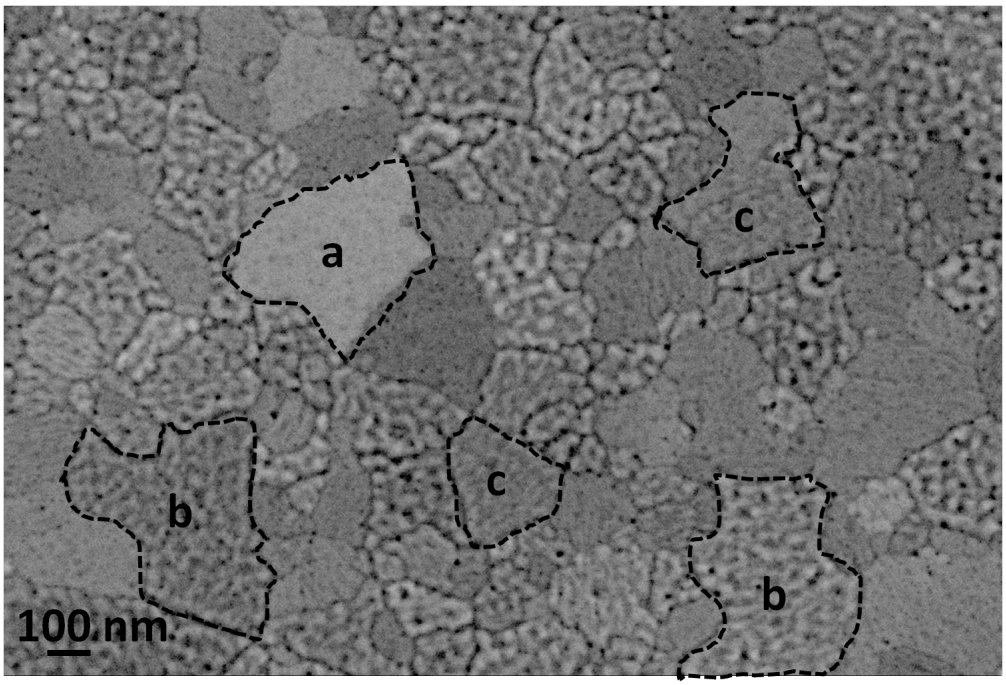

Fig.6

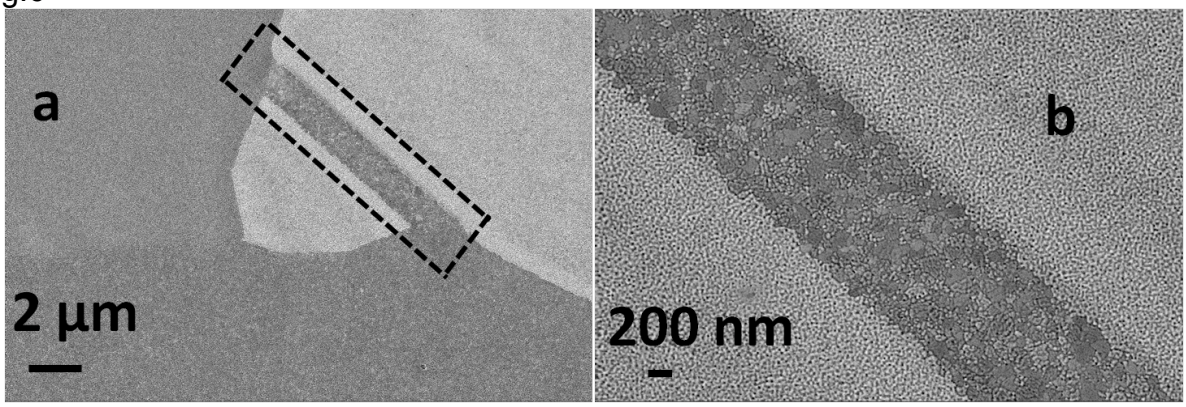

Fig.7

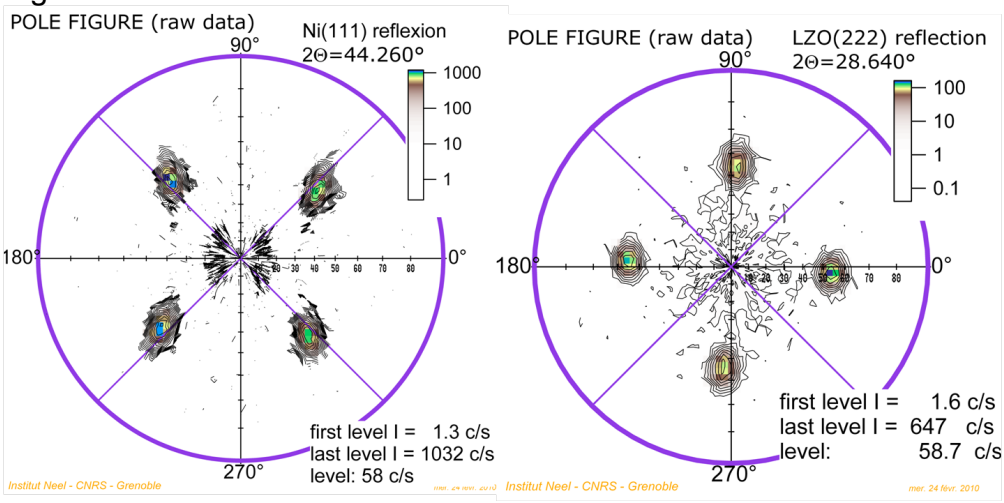

a b

Fig.8

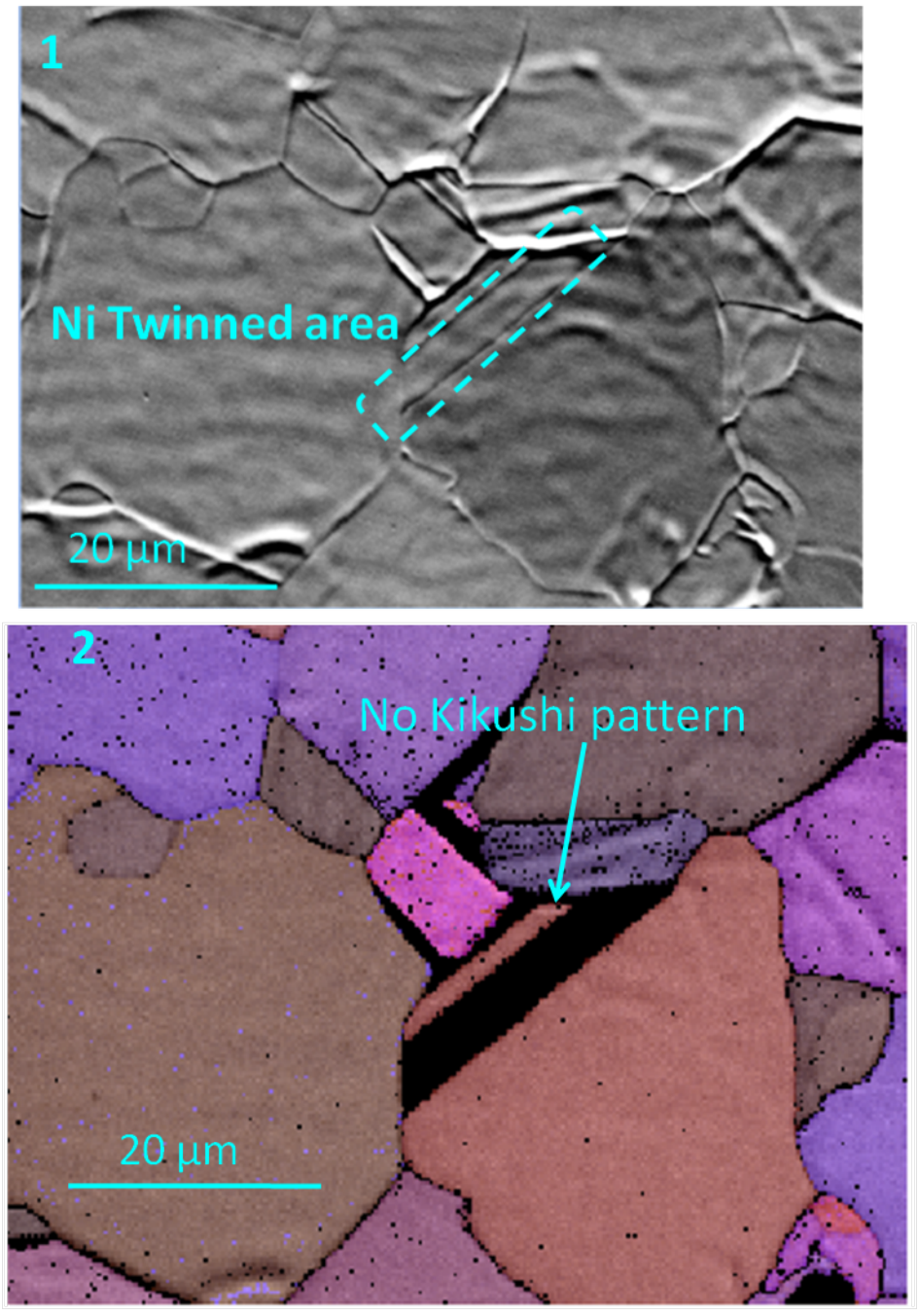

Fig.9

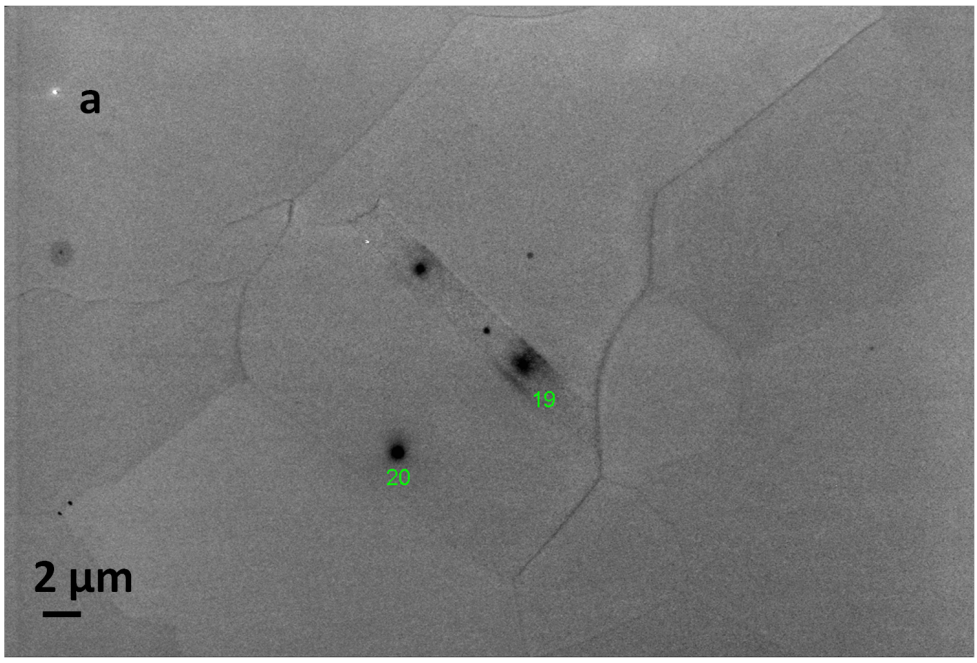

Fig.10a

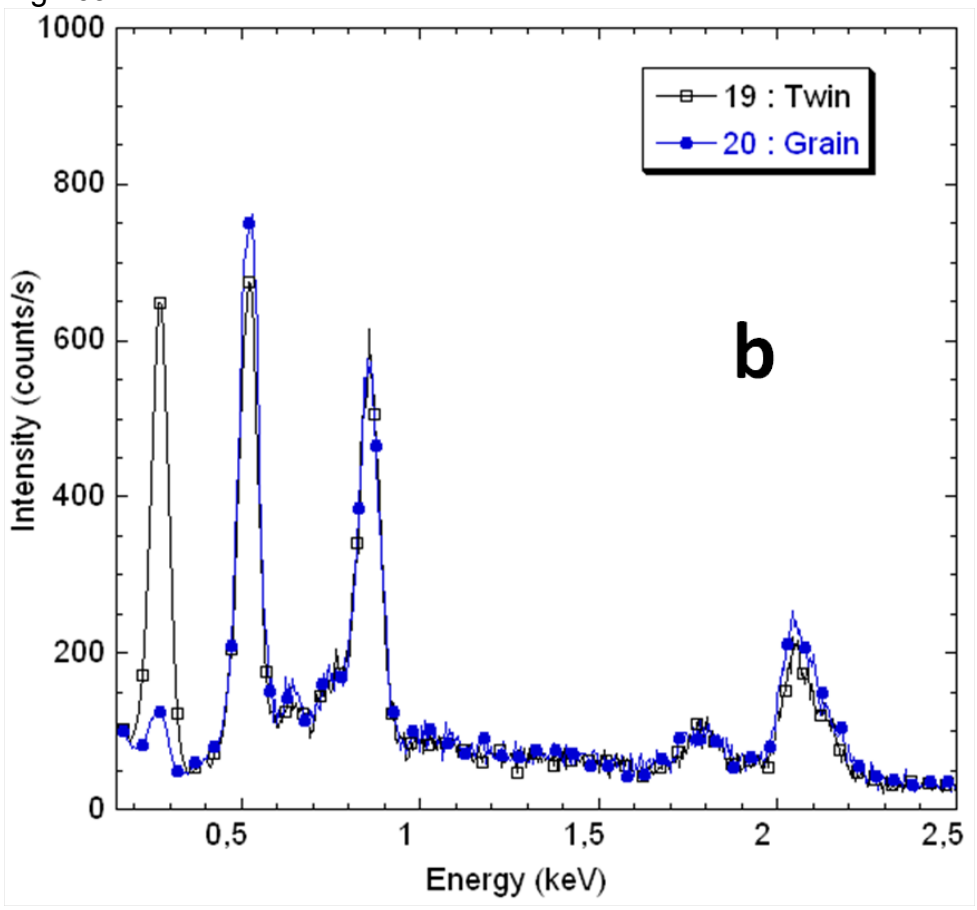

Fig.10b

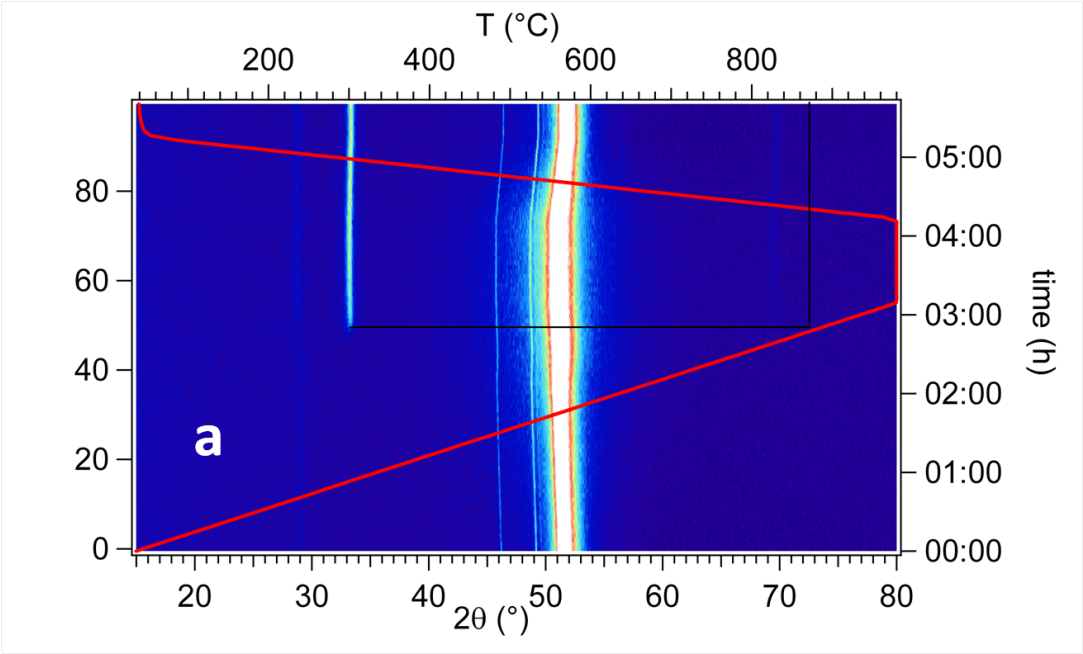

Fig.11a

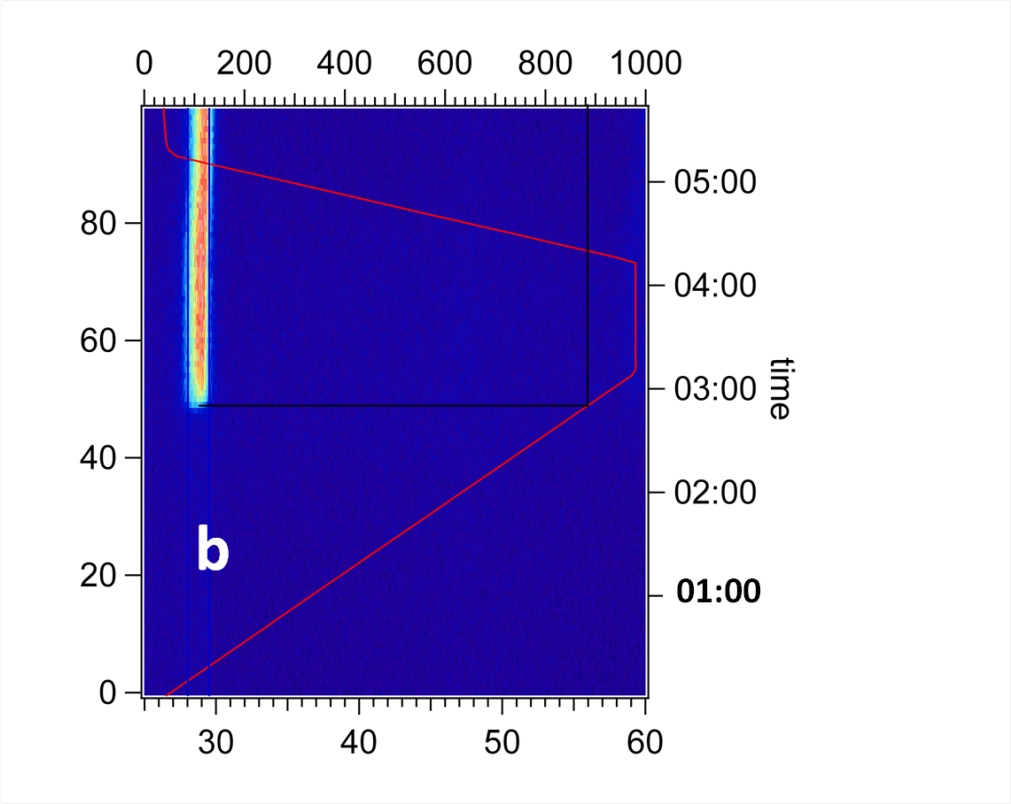

Fig.11b

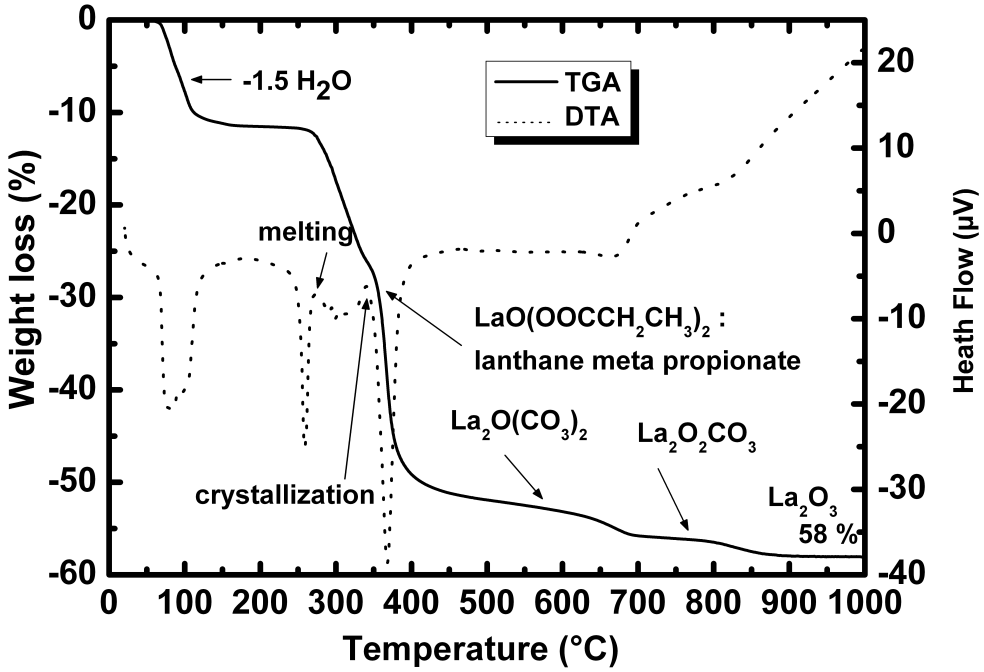
Weight loss (%)
Heath Flow (μV)
Temperature (°C)
-1.5 H2O
TGA
DTA
melting
crystallization
LaO(OOCCH2CH3)2 :
lanthane meta propionate
La2O(CO3)2
La2O2CO3
La2O3
58 %

Fig.12